ACCURATE POLARIZATION CALIBRATION AT 800 MHZ WITH THE GREEN BANK TELESCOPE

Yu-Wei Liao[1], Tzu-Ching Chang[1], Cheng-Yu Kuo[1,2], Kiyoshi Wesley Masui[3,4], Niels Oppermann[5], Ue-Li Pen[5], and Jeffrey B. Peterson[6]

ABSTRACT

Polarization leakage of foreground synchrotron emission is a critical issue in HI intensity mapping experiments. While the sought-after HI emission is unpolarized, polarized foregrounds such as Galactic and extragalactic synchrotron radiation, if coupled with instrumental impurity, can mimic or overwhelm the HI signals. In this paper we present the methodology for polarization calibration at 700-900 MHz, applied on data obtained from the Green Bank Telescope (GBT). We use astrophysical sources, both polarized and unpolarized sources including quasars and pulsars, as calibrators to characterize the polarization leakage and control systematic effects in our GBT HI intensity mapping project. The resulting fractional errors on polarization measurements on boresight are well controlled to within 0.6%-0.8% of their total intensity. The polarized beam patterns are measured by performing spider scans across both polarized quasars and pulsars. A dominant Stokes I to V leakage feature and secondary features of Stokes I to Q and I to U leakages in the 700-900 MHz frequency range are identified. These characterizations are important for separating foreground polarization leakage from the HI 21 cm signal.

Subject headings: Astronomical Instrumentation

1. INTRODUCTION

Neutral hydrogen (HI) is one of the most promising probes of the high-redshift universe. It can be used to uniquely trace the matter distribution at early times well into the dark ages and the cosmic dawn era, reveal the cosmic reionization process and shed light on the complex astrophysics in early galaxy formation, and probe the large-scale structure at late times, allowing measurements of the geometry and structure growth of the universe. To obtain statistical measurement of the three-dimensional structure of HI in emission, the intensity mapping technique has been advocated (e.g., Chang et al. (2008), Loeb & Wyithe (2008), Chang et al. (2010)). Making use of the redshifted 21 cm HI intensity mapping dataset obtained at the Green Bank Telescope (GBT), Masui et al. (2013) and Switzer et al. (2013) have measured the HI cross-power spectrum with the WiggleZ optical galaxies and reported limits on the HI auto-power spectrum, respectively, in the frequency range of 700-900 MHz or a redshifted HI range of $0.6 < z < 1$. Combining the cross-power and auto-power spectrum, the neutral hydrogen fluctuation amplitude, $\Omega_{HI}b_{HI}$ has been constrained as $\Omega_{HI}b_{HI} = [0.62^{+0.23}_{-0.15}] \times 10^{-3}$.

The main challenges of HI intensity mapping at these redshifts include synchrotron foreground radiation and man-made radio frequency interference (RFI). Localized synchrotron emission from extragalactic sources and diffuse synchrotron emission from the interstellar medium (ISM) in the Milky Way are the dominant astronomical foreground signals in the frequency range of interest. In the GBT HI observing fields reported by Switzer et al. (2013), which are at high Galactic latitudes, the synchrotron emission is still three orders of magnitude brighter than the 21 cm signals. However, synchrotron radiation is expected to be spectrally smooth (Oh and Mack (2003); Seo et al. (2010)). If all the instrumental effects, including calibration, spectral response, and primary beam pattern, are well understood and controlled, the synchrotron foregrounds will then have fewer degrees of freedom than the HI signals along the line of sight, or along the frequency direction, and can be separated. In the GBT data, RFI is found to be removable or controllable by flagging of frequency channels.

A crucial instrumental effect that needs to be controlled is polarization leakage. Although HI emission is considered unpolarized, the leakage of polarized synchrotron foreground emission into total intensity via imperfect instrumental response could introduce excess power and extra degrees of freedom into the observed intensity signal. Simulations suggest polarized intensity of Galactic Foregrounds can contain frequency structure via Faraday rotation induced by the ISM; leakages of such spectrally fluctuating polarization intensity into total intensity could thus mimic the HI signals along the frequency or redshift direction (Jelić et al. (2010), Moore et al. (2013)). Furthermore, polarization leakage itself may not be a smooth function of frequency. Therefore, one may not be able to simply separate polarization leakage from HI signals by isolating spectrally smooth patterns.

[1] Institute of Astronomy and Astrophysics, Academia Sinica, 11F of Astro-Math Building, AS/NTU, 1 Roosevelt Rd Sec. 4, Taipei 10617, Taiwan; ywliao@asiaa.sinica.edu.tw
[2] Department of Physics, National Sun Yat-Sen University, 70 Lienhai Road, Kaohsiung 80424, Taiwan
[3] Department of Physics and Astronomy, University of British Columbia, Vancouver, British Columbia, V6T 1Z1, Canada
[4] Canadian Institute for Advanced Research, CIFAR Program in Cosmology and Gravity, Toronto, Ontario, M5G 1Z8, Canada
[5] Canadian Institute for Theoretical Astrophysics, University of Toronto, 60 St. George Street, Toronto ON, M5S 3H8, Canada
[6] McWilliams Center for Cosmology, Carnegie Mellon University, Department of Physics, 5000 Forbes Ave., Pittsburgh PA 15213, USA

The polarized Galactic foreground is one to two orders of magnitude fainter than total intensity in regions with low Galactic synchrotron emission at the frequency of interest. The amplitude in total intensity due to polarization leakage would be comparable to that of the HI signals if the leakage fraction is at the percentage level, which is common in single dish radio telescopes (Martí-Vidal et al. 2012). Therefore, polarization calibration needs to be performed very carefully to eliminate the contamination from polarized foreground signals.

Recent investigation of LOFAR polarization leakage by Asad et al. (2015) provides a good estimate of polarization calibration errors (less than 0.005%) of inflicted on the HI signal of interest at 150 MHz. As an interferometer, the redundancy of LOFAR baselines dramatically reduces the integrated polarization calibration errors; this is however not the case for single dish telescopes. Besides, Moore et al. (2015) suggest that the foreground polarization fraction at ~ 150 MHz is one order of magnitude lower than that at 1.4 GHz. Polarization calibration with single dishes is potentially a challenge at 800 MHz.

Performing polarization calibration with a signal dish radio telescope with dual receptors, such as the GBT, usually entails determining the Jones matrix, which describes the instrumental response of the two polarization receptors to sky signals at each frequency channel. Polarized astrophysical sources are often used to solve for the Jones matrices (e.g.: Heiles (2001) and van Straten (2004)). PSRCHIVE (Hotan et al. (2004)), a software that is widely used for single dish radio polarization calibration in the pulsar community, uses pulsar observations at multiple parallactic angles to solve for the Jones matrix at each frequency channel. In this work, we use the Jones matrix model described by van Straten (2004), which is adopted in PSRCHIVE, to parametrize Jones matrices. We obtain both pulsar and quasar observations from the GBT. We first solve for the first-order approximation to the Jones matrix model parameters using pulsar data and the PSRCHIVE software, then fine tune the parameters using quasar observations. We begin with a brief introduction to GBT 800 MHz receiver and the back-end systems we use in this work in Section 2. The polarization calibration on boresight is discussed in detail in Section 3.

Besides polarization leakage on boresight, another key element is to characterize the polarized primary beam pattern of a telescope. Pulsar observations have the adventage that it is easy to separate on-axis pulsar signal and stationary off-axis leakage by subtracting off-pulse from on-pulse data. On the other hand, since both on-axis signal and off-axis leakage are stationary in our intensity mapping observations, off-axis leakage is therefore an issue that needs to be addressed. In Section 4, we use spider scans of quasars and pulsars to investigate the polarization beam pattern of the GBT. These patterns are important for the interpretation of the HI intensity mapping power spectrum. The procedure we are using to calibrate real data is summarized in Section 5. We will discuss the results and limits of our investigation in Section 6.

2. GBT 800 MHZ RECEIVER AND GUPPI BACKEND

Here we briefly describe the GBT 800 MHz receiver and backend system. The GBT has an off-axis optical design; the 800 MHz receiver is a prime-focus instrument that operates at 680-920 MHz. The feed is a corrugated feed horn with an Orthomode transducer (OMT) polarization splitter. There are known resonances associated with the OMT at 796.6 MHz and 817.4 MHz, which we omit from the analysis. A noise diode signal is injected after the OMT at 2 K level and switches at 15.26 Hz. We use the Green Bank Ultimate Pulsar Processing Instrument (GUPPI) pulsar back-end systems (DuPlain et al. 2008), with a bandwidth of 200 MHz (700-900 MHz) over 4096 frequency channels, and integrate over 1 ms intervals. GUPPI has the pulsar-folding capability which we use in our analysis. See Masui et al. (2013) for more details.

3. POLARIZATION CALIBRATION

In this section we present the method for polarization calibration at the beam center, or boresight, without considering the angular response of the primary beam. We adopt the model described by van Straten (2004) to parametrize the Jones matrix and use quasar and pulsar observations to find solutions for the Jones matrix parameters. We then apply the parameters on quasar data to further correct for polarization leakage.

3.1. Mueller/Jones matrix model

In the following sections we follow Britton (2000) and van Straten (2004) to model the Jones matrix. The mapping between the real sky electric field signal $\boldsymbol{S}_{\mathrm{E}} = (E_x, E_y)$ and the observed signal $\boldsymbol{S}'_{\mathrm{E}} = (E'_x, E'_y)$ through an instrument is

$$\boldsymbol{S}'_{\mathrm{E}} = \mathbf{J}\mathbf{R}_{\mathrm{E}}(\phi)\boldsymbol{S}_{\mathrm{E}}, \qquad (1)$$

where $\mathbf{J}$, which is typically called Jones matrix, is the instrumental response, and

$$\mathbf{R}_{\mathrm{E}}(\phi) = \begin{pmatrix} \cos\phi & \sin\phi \\ -\sin\phi & \cos\phi \end{pmatrix} \qquad (2)$$

is the relative rotation between the sky and the receptor by a parallactic angle ϕ. If we transform Eqn. (1) into the basis of Stokes parameters, we get

$$\boldsymbol{S}'_{\mathrm{sp}} = \mathbf{M}\mathbf{R}(\phi)\boldsymbol{S}_{\mathrm{sp}}, \qquad (3)$$

where $\boldsymbol{S}_{\mathrm{sp}}$ is a 4-vector representing Stokes (I, Q, U, V), $\mathbf{M}$ the 4×4 Mueller matrix, and

$$\mathbf{R} = \begin{pmatrix} 1 & 0 & 0 & 0 \\ 0 & \cos 2\phi & \sin 2\phi & 0 \\ 0 & -\sin 2\phi & \cos 2\phi & 0 \\ 0 & 0 & 0 & 1 \end{pmatrix}. \qquad (4)$$

Note the relation between the 2-vector $\boldsymbol{S}_{\mathrm{E}}$ and 4-vector $\boldsymbol{S}_{\mathrm{sp}}$ is

$$\boldsymbol{S}_{\mathrm{sp}} = \mathbf{A}(\boldsymbol{S}_{\mathrm{E}} \otimes \boldsymbol{S}_{\mathrm{E}}^*), \qquad (5)$$

where $\otimes$ is Kronecker product and

$$\mathbf{A} = \begin{pmatrix} 1 & 0 & 0 & 1 \\ 1 & 0 & 0 & -1 \\ 0 & 1 & 1 & 0 \\ 0 & i & -i & 0 \end{pmatrix}. \qquad (6)$$

The relation between the Jones matrix $\mathbf{J}$ and Mueller matrix $\mathbf{M}$ is then

$$\mathbf{M} = \mathbf{A}(\mathbf{J} \otimes \mathbf{J}^*)\mathbf{A}^{-1}. \tag{7}$$

$\mathbf{J}$ can be parametrized as

$$\mathbf{J} = G\mathbf{\Gamma}(\gamma)\mathbf{R}_\Phi(\varphi)\mathbf{C}, \tag{8}$$

where G, the absolute gain, is a scalar. $\mathbf{\Gamma}(\gamma)$ is a matrix corresponding to the differential gain γ,

$$\mathbf{\Gamma}(\gamma) = \begin{pmatrix} e^\gamma & 0 \\ 0 & e^{-\gamma} \end{pmatrix}. \tag{9}$$

$\mathbf{R}_\Phi(\varphi)$ is a matrix corresponding to the differential phase φ,

$$\mathbf{R}_\Phi(\varphi) = \begin{pmatrix} e^{i\varphi} & 0 \\ 0 & e^{-i\varphi} \end{pmatrix}. \tag{10}$$

$\mathbf{C}$ is a matrix that represents a receiver with non-orthogonal receptors,

$$\mathbf{C} = \delta_0 \mathbf{L}(\theta_0, \epsilon_0) + \delta_1 \mathbf{L}(\theta_1, \epsilon_1), \tag{11}$$

where $\mathbf{L}(\theta, \epsilon)$ is written as

$$\mathbf{L}(\theta, \epsilon) = \begin{pmatrix} \cos\epsilon & i\sin\epsilon \\ i\sin\epsilon & \cos\epsilon \end{pmatrix} \begin{pmatrix} \cos\theta & \sin\theta \\ -\sin\theta & \cos\theta \end{pmatrix}. \tag{12}$$

ϵ and θ are the ellipticity and orientation of the receptor, respectively. δ_a is the selection matrix,

$$\delta_a = \begin{pmatrix} \delta_{0a} & 0 \\ 0 & \delta_{1a} \end{pmatrix}, \tag{13}$$

where δ_{ab} is the Kronecker delta.

$\mathbf{C}$ can be decomposed as

$$\mathbf{C}(\epsilon_0, \theta_0, \epsilon_1, \theta_1) = \mathbf{C}(\epsilon_0, \theta_0 - \phi_0, \epsilon_1, \theta_1 - \phi_0)\mathbf{R}_E(\phi_0), \tag{14}$$

where

$$\mathbf{R}_E(\phi_0) = \begin{pmatrix} \cos\phi_0 & \sin\phi_0 \\ -\sin\phi_0 & \cos\phi_0 \end{pmatrix} \tag{15}$$

is equivalent to the parallactic angle rotation. Therefore, one can define $\theta_+ \equiv \theta_0 + \theta_1$ and $\theta_- \equiv \theta_0 - \theta_1$ to separate the overall rotation from the relative rotation between receptors, and merge θ_+ into parallactic angle rotation.

Then one can transform $\mathbf{J}$ to Mueller matrix $\mathbf{M}$ with Eqn. (7).

To illustrate some of the structure of the Jones and Mueller matrices, we set $(\theta_0, \theta_1, \epsilon_0, \epsilon_1) = 0$, Eqn. (8) can be rewritten as:

$$\mathbf{J} = G \begin{pmatrix} e^{\gamma + i\varphi} & 0 \\ 0 & e^{-\gamma - i\varphi} \end{pmatrix}, \tag{16}$$

and the Mueller matrix becomes

$$\mathbf{M_0} = G^2 \begin{pmatrix} \cosh(2\gamma) & \sinh(2\gamma) & 0 & 0 \\ \sinh(2\gamma) & \cosh(2\gamma) & 0 & 0 \\ 0 & 0 & \cos 2\varphi & \sin 2\varphi \\ 0 & 0 & -\sin 2\varphi & \cos 2\varphi \end{pmatrix}. \tag{17}$$

In summary, the Jones matrix is a 2×2 complex matrix, in principle it has eight degrees of freedom. However, from Eqn. (7), one can see that the absolute phase of $\mathbf{J}$ does not affect the Mueller matrix $\mathbf{M}$. Therefore, the complete Jones/Mueller matrix model can be described by seven parameters, which are the absolute gain G, the differential gain γ, the differential phase φ, θ_0, θ_1 the orientation of the two receptors, and the ellipticity of the receptors ϵ_0, ϵ_1.

3.2. Polarization calibration with pulsar

3.2.1. Solving Mueller matrix with Pulsar data

One can observe a polarized source, such as a pulsar, to measure $\boldsymbol{S}'_E$ at parallactic angle ϕ. With data taken at several parallactic angles, one will have a set of simultaneous equations, $\boldsymbol{S}'_{Ei} = \mathbf{J}\mathbf{R}_E(\phi_i)\boldsymbol{S}_E$, or

$$\boldsymbol{S}'_{spi} = \mathbf{M}\mathbf{R}(\phi_i)\boldsymbol{S}_{sp} \tag{18}$$

in the Stokes parameter basis. i indexes the observation at parallactic angle ϕ_i

Before solving for both the incoming signals of the pulsar and the Jones matrix parameters using these equations, we have to deal with two degeneracies: One of the degeneracies is between the Stokes parameters I and V of the incoming signal, and the other is between Stokes Q and U.

The degeneracies arise from the following: In Eqn. (18), one can equally substitute $\mathbf{M}$ and $\boldsymbol{S}_{sp}$ with $\mathbf{M}\mathbf{D}^{-1}$ and $\mathbf{D}\boldsymbol{S}_{sp}$, respectively, as long as the matrix $\mathbf{D}$ commutes with $\mathbf{R}$. In other words, if $\boldsymbol{S}_{sp}$ is one solution of Eqn. (18), $\mathbf{D}\boldsymbol{S}_{sp}$ will be another solution as well. In fact, any matrix $\mathbf{D}$ of the following form,

$$\mathbf{D} = a \begin{pmatrix} 1 & 0 & 0 & V_1 \\ 0 & 1 & 0 & 0 \\ 0 & 0 & 1 & 0 \\ V_2 & 0 & 0 & 1 \end{pmatrix} + b \begin{pmatrix} 1 & 0 & 0 & 0 \\ 0 & \cos\theta & \sin\theta & 0 \\ 0 & -\sin\theta & \cos\theta & 0 \\ 0 & 0 & 0 & 1 \end{pmatrix}, \tag{19}$$

will commute with $\mathbf{R}$ (see Appendix B of van Straten (2004)). The first term of Eqn. (19) corresponds to degeneracy between I and V, and the second term degeneracy between Q and U.

One way to break the degeneracy between Stokes I and V is to observe a standard calibrator with a known ratio of Stokes I to V. There is a built-in noise diode at the GBT that can serve this function. Ideally, the noise diode will produce pure linearly polarized signals at a position angle $45°$ to the two orthogonal receptors. We can therefore break the degeneracy between Stokes I and V by assuming that the noise diode produces no circular polarization signals. Alternatively, we can assume the system circular polarization V to be negligible while observing astrophysical calibrators.

As is the standard procedure, by taking the differences of on- and off-source observations of a standard calibrator, such as 3C295, one can estimate its circular polarization. One can therefore break the degeneracy by assuming the Stokes V of standard calibrators, which are reported to have a negligible level of V, to be zero.

The degeneracy between Q and U, which makes it impossible to calibrate absolute polarization angles on the sky without an external reference, is related to the definition of angles. Here we set the orientation of the first receptor by fixing $\theta_0 = 0$. Therefore, $\theta_- = -\theta_1$ in the following sections.

PSRCHIVE solves $\mathbf{J}$ by using a least-squares minimization method for each frequency channel (see van Straten

(2004) for more detail). It automatically selects several pulsar pulse phase bins, from pulsar data taken at different parallactic angles, to solve for the model parameters. The unknown variables are the Stokes parameters of the incoming pulsar signals and the Jones matrix parameters of the instrument. Because the total flux density I of pulsars typically varies on a time-scale of minutes, PSRCHIVE normalizes the Stokes parameters by the invariant interval $S = I^2 - Q^2 - U^2 - V^2$ instead (details in van Straten (2004)). We can therefore compare pulsar Stokes parameters between different scans.

However, the PSRCHIVE does not directly assume the circular polarization of the standard candle to be zero. Instead, PSRCHIVE provides two options: either assume the V of system temperature while directing the telescope to a standard candle , or the V of noise diode, to be zero. Following van Straten (2004), who suggests that the circular polarization of a noise diode is significantly different from zero, we choose the first option.

With pulsar observations at five different parallactic angles, we have 20 measurements (4 polarizations × 5 parallactic angles) at each frequency channel and each selected pulse phase bin. In addition to the flux calibrator data from quasar observations (four polarizations) and the noise diode data (four polarizations), we have 328 measurements for 16 selected pulse phase bins at each frequency channel. The number of variables at each frequency is 76, including a total of 64 Stokes parameters of the pulsar for the 16 selected pulse phase bins, six Stokes parameters of the flux calibrator and noise diode (the I of flux calibrator is assumed to be known, and the V of flux calibrator is set to be zero), and six instrumental Jones/Mueller matrix model parameters (i.e., the seven parameters describe in Section 3.1 except for θ_0, which is set to be 0 to break the degeneracy between Q and U). Once PSRCHIVE obtains the best fit instrumental parameters, it generates both the Jones matrix and Mueller matrix for each frequency channel with the formalism described in the above section.

Figures 1 and 2 show the Jones matrix obtained from pulsar data, where we took five five-minute tracking scans for pulsar B1133+16 in Jan, 2014 at different parallactic angles with the GBT. The standard candle used is quasar 3C295, which is known to be an unpolarized source at 800 MHz. The model parameters shown in Figure 2 are consistent with the ones shown by Han et al. (2009) in the overall.

3.2.2. *Determining parameters with noise diode*

We find that at the GBT, the value of φ changes dramatically day by day and needs to be determined with each observation; the values of G and γ are also found to change slightly day by day and significantly several times in a observing semester over six months.

Since at the GBT, the noise diode signal is injected into the receiver only after the separation of orthogonal polarizations, parameters $\epsilon_{0,1}$ and $\theta_{0,1}$, which describe the cross-talk between orthogonal polarizations, are expected to be negligible for noise diode signal. The Mueller matrix that applies to the noise diode signal can thus be written as Eqn. (17).

One can therefore solve for G, γ, and φ by inserting a known noise diode standard profile $\boldsymbol{S}_{\mathrm{ncal}}$ and the ob-
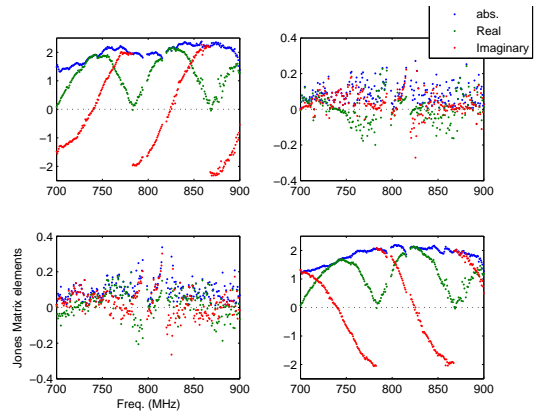

FIG. 1.— The Jones matrix elements of GBT as a function of frequency. The upper left is $\mathbf{J}(0,0)$, upper right $\mathbf{J}(0,1)$, lower left $\mathbf{J}(1,0)$, and lower right $\mathbf{J}(1,1)$. The Jones matrix is obtained from B1133+16 data. The unit is arbitrary. The features nears frequencies 800 MHz and 820 MHz are due to the resonance in the orthomode transducer (OMT) in this band at the GBT, and are excluded from all analysis in this paper.
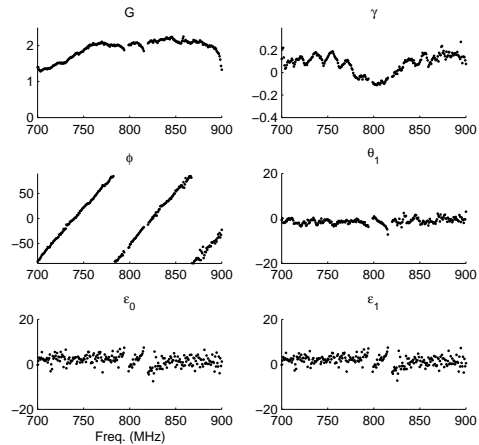

FIG. 2.— The values of Jones matrix parameters of GBT as a function of frequency. The parameters are obtained from B1133+16 data. The unit of G is abitrary, γ is dimensionless. φ, θ_1, ϵ_0, and ϵ_1 are in units of degree.

served noise diode data $\boldsymbol{S}'_{\mathrm{ncal}}$ into

$$\mathbf{M_0}\boldsymbol{S}_{\mathrm{ncal}} = \boldsymbol{S}'_{\mathrm{ncal}}. \tag{20}$$

Assuming the noise diode frequency profile is stable over a few months, we can use the noise diode data calibrated by PSRCHIVE as the standard profile to solve for G, γ, and φ for each observation session. Combining these parameters with θ_1, ϵ_0, and ϵ_1 obtained from multiple parallactic-angle tracking scans of B1133+16, we can achieve $\sim 1.3\%$ accuracy on all the Stokes parameters, with respect to total intensity, of the unpolarized quasar 3C147. The accuracy of 1.3% is the RMS fluctuation of dozens of calibrated tracking scans on 3C147 over an entire semester.

3.3. *Parameter modification with Quasar data*
3.3.1. *Previous Assumptions*

The calibration method described above is based on the following assumption: The linear polarization frac-

tion, angle, and the circular polarization fraction of the target pulsar are assumed to be stable over the observation period, which is about six hours. To test the first assumption, we examine the calibrated pulsar properties as a function of time. Figure 3 shows the RMS of linear polarization fraction over five calibrated pulsar tracking scans taken in the same night. We find that the RMS fluctuation of the linear polarization fraction measured over multiple parallactic-angle pulsar tracking scans is higher than the thermal noise level. It appears the polarization fraction of pulsars is not stable enough for our purpose. The RMS fluctuation of the linear polarization angle ($\approx 2°$-$4°$) and circular polarization fraction ($\approx 1\%$-3%) are also larger than acceptable.

Because it takes a good amount of observing time (including overhead) to conduct multiple parallactic angle pulsar tracking scans, during our HI intensity mapping observing campaign spread over a few semesters, we only take multiple parallactic-angle pulsar tracking scans once every several months. The stability of the noise diode profile becomes crucial. The stability is tested with observations of on- and off-source quasar tracking scans while blinking the thermal noise diode at 15.26 Hz in every observing session. Comparing data with and without a bright quasar in the center of the beam, and data with and without the noise diode signal, one can derive T_x and T_y, the injected noise diode temperature in the two polarization directions, given the known spectrum of the quasar. We find that the noise diode is not stable over a time span of six months either. Figure 4 shows noise diode temperature measured with scans on 3C48 in 2011. There appears to be a discontinuity in noise diode temperature at scan 22, below which the receptor X has a higher temperature than receptor Y but with a 2dB attenuation above 840 MHz. This discontinuity was observed between June 27, 2011 and July 17, 2011, which coincided with the maintenance activity at the GBT when the 800 MHz receiver was taken down from the prime focus. It is quite possible that the noise diode was reset when the receiver reinstalled. Therefore, we need to modify the method of estimating the Jones/Mueller matrix for the GBT.

3.3.2. *Noise Diode Behavior*

In order to reduce the impact of noise diode instability, we examine T_x and T_y as a function of time and frequency, derived from quasar tracking scans in each session, then group all sessions into subsets according to the shapes of the derived noise diode frequency profiles. In practice, the number of identified noise diode profile shapes in each semester varies between 1 to 9 for the five semesters from 2011 to 2015. We average the $T_x(\nu)$ and $T_y(\nu)$ profiles within each subset to obtain $\tilde{T}_{x,j}(\nu)$ and $\tilde{T}_{y,j}(\nu)$, where j indexes subsets. Then we normalize the profiles to $\left\langle \sqrt{\tilde{T}_{x,j}\tilde{T}_{y,j}} \right\rangle_\nu = 1$, averaging over all frequency channels. We further average $\left\langle \sqrt{T_x T_y} \right\rangle_\nu$ over all tracking scans within each session to get a normalization factor N_k for each session, where k indexes sessions. Finally we obtain estimated noise diode profile for each session as $N_k \tilde{T}_{x,j}$ and $N_k \tilde{T}_{y,j}$, then apply them to correct $\boldsymbol{S}_{\mathrm{ncal}}$ in Eqn. (20). In order to reduce the impact

of errors associated with the estimation of noise diode profiles, we only allow $\langle T_x T_y \rangle_\nu$ to vary between sessions, and fix the profile shape within each subset.

3.3.3. *First-order Correction*

Assuming $\theta_1, \epsilon_0, \epsilon_1 \ll 1$, to first-order approximation we can calculate the resulting calibration errors induced by errors in values of Jones matrix parameters using Eqn. (A1) and (A3). The formalism is described in detail in Appendix A. Figure 2 suggests that the assumption of small θ_1, ϵ_0, and ϵ_1 values is sound for the GBT. We can also define $\epsilon_+ \equiv \epsilon_0 + \epsilon_1$ and $\epsilon_- \equiv \epsilon_0 - \epsilon_1$, for they are directly associate with Q-V and I-V leakages, respectively (see Appendix A and Britton (2000)).

For an unpolarized source like quasar 3C295, one can apply $\boldsymbol{S}_{\mathbf{sp}} = [I, 0, 0, 0]$ to Eqn. (A1) and (A3), and get

$$\delta Q/I = -(2\delta\gamma\cos 2\phi - \delta\theta_- \sin 2\phi) \qquad (21)$$

and

$$\delta U/I = -\delta\theta_- \cos 2\phi - 2\delta\gamma\sin 2\phi. \qquad (22)$$

These equations predict a sinusoidal dependence of the calibrated Q and U on parallactic angles. The predicted sinusoidal pattern is shown as blue dots in Figure 5, which represent the Q and U values of 3C295 data calibrated with a Mueller matrix calculated from pulsar observations,

For an unpolarized source, the calibrated values of Q and U, which are otherwise expected to be zero with perfect polarization calibration, are denoted as δQ and δU. Substituting these values into Eqns. (21) and (22), we obtain the best-fit values of $\delta\gamma$ and $\delta\theta_-$.

As a consistency check, we calculate the values of $\delta\gamma$ and $\delta\theta_-$ with data on 3C147, adjust the γ and θ_- parameters accordingly and apply them to the polarization calibration of 3C295 data. The 3C295 data calibrated with the modified parameters are shown as green and red dots in Figure 5. Modification of γ and θ_- dramatically reduce the fluctuation of calibrated Q and U of 3C295. This implies the modification of γ and θ_- parameters is a sound approach.

On the other hand, the matrix element $(4, 1)$ in the right hand side of Eqn. (A3) describes the leakage from I into V due to $\delta\epsilon_-$. The circular polarization level of 3C295 is smaller than 0.6% at our frequency band, thus we assume that the oscillating pattern of V of calibrated 3C295 data, which is shown as the blue curve in Figure 6, is caused by $\delta\epsilon_-$ in the parameter set we applied. Just as for $\delta\theta_-$ and $\delta\gamma$, we also use a modified ϵ_- derived from 3C147 data to calibrate 3C295 data. The corrected V of 3C295 is much closer to zero as shown by the green curve in Figure 6.

Once we obtain the modified γ, θ_-, and ϵ_- from quasar data, one can apply the solutions to other quasars including 3C48, 3C295, 3C147, and 3C286. The RMS of calibrated stokes parameters over dozens of tracking scans through an entire observing semester are about 0.6%-0.8% of the quasar intensity in most of the frequency channels. 3C286, a slightly polarized quasar, is taken as an example to illustrate the outcome of the parameter correction, indicated by the blue and green lines in Figure 7.

The modified θ_- can be used to test the assumption that the cross talk between T_x and T_y of the noise diode

is negligible. As shown in Eqn. (A2), θ_- describes the leakage between I and U. The θ_- experienced by the sky signal can be approximated as a linear combination of θ_- before and after noise diode signal injection. We denote the latter one as $\theta_{-,\mathrm{ncal}}$ because it is the $\theta-$ which noise diode signal experienced. As U_{ncal} is strong ($\approx 80\%$ of I_{ncal}), fluctuations in $\theta_{-,\mathrm{ncal}}$ will contribute to the fluctuations in I_{ncal}. Therefore, we postulate that the measured I_{ncal} is to correlate with the θ_- value estimated from quasar data, if the fluctuation of $\theta_{-,\mathrm{ncal}}$ is not negligible.

We therefore correlate fluctuations over time and frequency channels of I_{ncal} and θ_- obtained from quasar 3C48 taken in 2014 and 2015. The most prominent patterns extracted using singular-value decomposition in frequency-time space are removed before correlation. These removed patterns of I_{ncal} and θ_- do not correlate with each other. On the other hand, from previous noise diode data, we found that $T_{x,\mathrm{ncal}}$ and $T_{y,\mathrm{ncal}}$ tend to preserve spectral shape over several nights with normalization changes each night. This kind of pattern matches what we get in the first SVD mode. These two facts imply that these removed modes can be considered to represent fluctuations of I_{ncal} and θ_- before the light path of sky signal merge with the noise diode signal. The residual I_{ncal} and θ_- have a correlation coefficient of $r = 0.24 \pm 0.03$, significantly different from 0. As a sanity check, we remove the correlated part from I_{ncal}, and find the RMS of measured I_{ncal} only reduced by $\approx 0.04\%$ of total I_{ncal}. Although there is statistically significant correlation between residual I_{ncal} and θ_-, the impact of this correlation is much smaller than the uncertainty level, 0.6%-0.8%, of our calibration. We perform a similar check on ϵ_- and noise diode V_{ncal}, for $\delta\epsilon_-$ would results in leakage from I_{ncal} into V_{ncal} if $\delta\epsilon_-$ happens after noise diode signal injecting into the receiver. We do not find significant correlation between ϵ_- and the V_{ncal}. We therefore conclude that the cross talk between $T_{x,\mathrm{ncal}}$ and $T_{y,\mathrm{ncal}}$ is negligible.

3.4. *Ionospheric Rotation Measure Correction*

Ionospheric Faraday rotation is another effect that needs to be accounted for in the data. Faraday rotation is the rotation of linear polarization direction when photons propagate through magnetized free electrons. The angle of rotation is proportional to the wavelength λ of light as λ^2, and can be written as $\theta_{\mathrm{FR}} = \phi_{\mathrm{RM}}\lambda^2$, where ϕ_{RM} is Rotation Measure (RM). RM can be calculated as

$$\phi_{\mathrm{RM}} \approx (2.62 \times 10^{-13}\mathrm{T}^{-1}) \int n_{\mathrm{e}}(s)B_{\parallel}(s)ds, \quad (23)$$

where n_{e} is free electron density, $B_{\parallel}$ is the strength of magnetic field component parallel to the line of sight, T stands for Tesla, the SI unit magnetic field strength, and ds is integrated along the line of sight.

Photons from astronomical sources propagate through the terrestrial ionosphere, composed of the free electrons magnetized by the geomagnetic field, the linear polarization angle of light is thus rotated by the Faraday effect. The RM depends on the spatial distribution of n_e, which is a function of time, and the trajectory of light propagation, which is determined by azimuth and elevation of the pointing of the telescope. We adopt empirical orthonormal functions (EOFs)(Fuller-Rowell et al. 2006) and incorporate ionospheric information released by US-TEC (Fuller-Rowell et al. (2006) and Araujo-Pradere et al. (2007)) to estimate free electron density at the time of observation. The geomagnetic field is calculated using the International Geomagnetic Reference Field (IGRF) (Finlay et al. 2010). After applying the free electron number density and geomagnetic field to Eqn. (23), we obtain the RM values and calculate θ_{FR} caused by ionospheric free electrons. Faraday rotation can be corrected by simply adding θ_{FR} to the parallactic rotation angle ϕ in Eqn. (4).

With $\phi_{\mathrm{RM}} = 2m^{-2}$, which is a typical ionospheric ϕ_{RM} value at the GBT site during night time when we observe, θ_{FR} is 12.7° at 900 MHz and 21.0° at 700 MHz. The ionospheric Faraday rotation affects the linear polarization direction rather significantly in our observing frequency range.

Figure 8 shows the comparison of RM values fitted as the slope of linear polarization angles with respect to λ^2 using calibrated 3C286 data, the phase angles of calibrated 3C286 data averaged over frequency channels, and estimated ionospheric RM. The right panel of Figure 8 shows that our RM correction effectively reduces the fluctuation of polarization angle over time.

In principle, the remaining RM after ionospheric RM correction should be the RM of the celestial object. However, it is reported that the RM of 3C286 is very close to zero (Perley and Butler 2013), which significantly differs from what we measure in Figure 8. Note though that the FWHM of the GBT beam in our frequency band is about $15' - 19'$, the on-source 3C286 data will thus include contributions from the surrounding Galactic Foreground. Although we subtract off-source data, which is taken 3 degrees away from 3C286, the Galactic foreground at these two patches may differ and affect the estimated RM value.

We have therefore taken 33 tracking scans of pulsar B1929+10. We eliminate Galactic foreground RM contribution by gating the pulsar and subtracting off-pulse from on-pulse data, and expect the pulsar RM measurement to be free of Galactic foreground contamination. After ionospheric RM correction, the pulsar RM calculated from the slope of $arg(Q + iU)$ changes from $-5.9 \pm 0.3m^{-2}$ to $-7.1 \pm 0.3m^{-2}$, which is consistent with the RM value from the literature, $-6.9m^{-2}$ (Johnston et al. 2005). We therefore validate our ionospheric RM correction procedure.

4. POLARIZED BEAM RESPONSE

In the previous section we have focused on on-axis (boresight) polarization calibration only. However, off-axis polarization leakage can potentially contaminate HI intensity maps and power spectrum estimation. Considering the full polarized beam response, Eqn. (3) should be rewritten as a convolution,

$$\boldsymbol{S'}(\vec{x}) = \int \mathbf{M}(\Delta\vec{x})\mathbf{R}(\phi)\boldsymbol{S}(\vec{x'})d^2x', \quad (24)$$

where $\vec{x}$ and $\vec{x'}$ are the two-dimensional positions in the sky, $\Delta\vec{x} = \vec{x'} - \vec{x}$. $\vec{x}$ and $\vec{x'}$ are defined in horizontal coordinate system. $\vec{x}$ is the position of the boresight
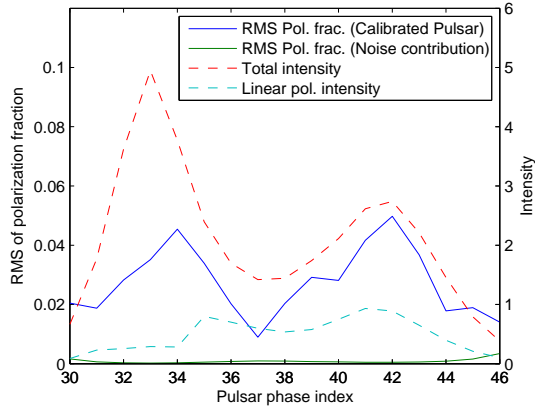
FIG. 3.— The RMS of linear polarization fraction of pulsar B1133+16. The X axis is pulsar phase index. The blue curve is derived by comparing 5 tracking scans on B1133+16 taken at the same night. The green curve shows the contribution of noise. The dashed lines show the total and linear polarization intensity of the pulsar. The unit of intensities is arbitrarily.
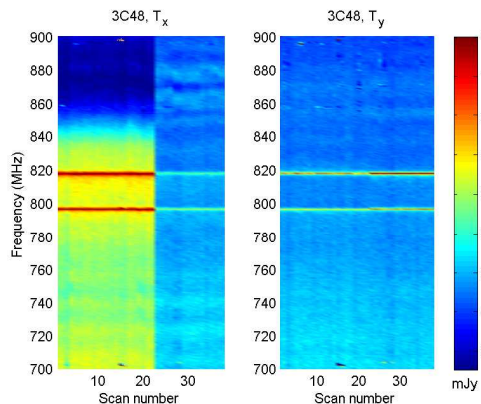

FIG. 4.— An example of instability of GBT noise diode. In this figure we show the T_x and T_y of noise diode derived by comparing noise diode data with 3C48 data, which were taken at the same time. The left panel and right panel are T_x and T_y of noise diode, respectively. The intensity unit here is mJy. The dataset shown here consists 38 tracking scans spreading from May to August, 2011. The two horizontal stripes at frequencies near 800 MHz and 820 MHz correspond to bad channels due to the resonance in the orthomode transducer (OMT) in this band at the GBT, and are excluded from all analysis.

and $\vec{x'}$ the position of the source on the sky, so that $\Delta\vec{x}$ represents the source position relative to the boresight on the sky. In the case of a point source, where $\boldsymbol{S}(\vec{x'}) = \boldsymbol{S_0}\delta(\vec{x'} - \vec{x_0})$, Eqn. (24) reduces to Eqn. (3) with $\mathbf{M} = \mathbf{M}(\vec{x_0} - \vec{x})$. In this section we use quasars and pulsars as probes to investigate the feature of $\mathbf{M}(\Delta\vec{x})$. We also discuss the advantages and weaknesses of these two types of targets for polarization calibration.

4.1. *Polarized Beam from Quasar spider scans*
4.1.1. *Polarized Beam Pattern*

We perform the so-called 'spider scans' on unpolarized quasars to investigate the structure of the first column of the Mueller matrix $\mathbf{M}(\Delta\vec{x})$, i.e., the leakage contributions from intensity to polarization. To conduct a spider scan, we slew the telescope along four $1°$ paths across the central source: one of the four paths is iso-azimuthal,
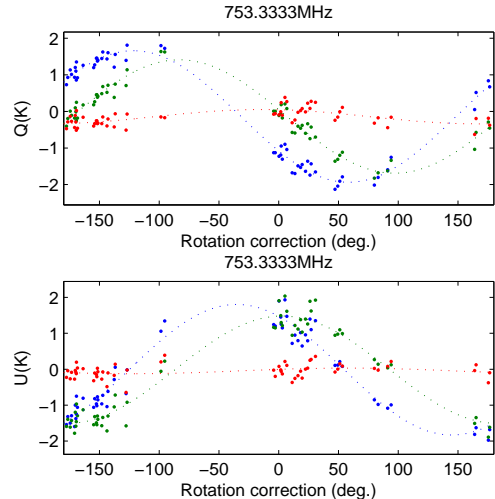

FIG. 5.— Comparison of calibrated Q (upper) and U (lower) of an unpolarized source 3C295 with/without parameter modifications. The blue dots show the data calibrated by the method described in Section 3.2, the green dots are calibrated with modified γ, and the red ones are calibrated with modified γ and θ_-. Each dot corresponds to one 1-minute tracking on 3C295. The parameter modification is described in Section 3.3.3. The rotation correction here is defined as 2ϕ. The total intensity of 3C295 in frequency range 700 - 900 MHz spread from 58 K to 72 K.
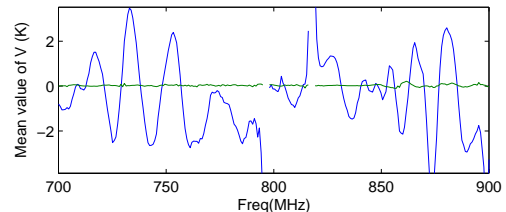

FIG. 6.— Calibrated V of 3C295. The blue curve shows the calibrated V from pulsar tracking scans, and the green curve includes the ϵ_- correction with data from 3C147, which helps substantially in achieving $V \sim 0$. The total intensity of 3C295 in frequency range 700 - 900 MHz spread from 58 K to 72 K.

one iso-elevation, and the other two are $45°$ from the first two (shown as black lines in the upper panels of Figure 9). The lengths of the paths are 4.0 and 3.2 times of the beam FWHM at 900 MHz and 700 MHz, respectively. We select a few unpolarized quasars, including 3C48, 3C295, and 3C147, as targets. The upper panels of Figure 9 show the beam maps from direct interpolation of 3C295 spider scans at a single frequency channel. The data shown in Figure 9 have been calibrated with the boresight calibration method described in Section 3.

In order to quantify the resulted polarization beams and minimize the impact of observational noise, we model the spider scan maps with the two-dimensional Gauss-Hermite functions, which are perturbations around a two-dimensional Gaussian profile. The 2D Gauss-Hermite function is written as

$$\mu_{ij}\left(\frac{x}{x_0}, \frac{y}{y_0}\right) = e^{\frac{-(x^2+y^2)}{2\sigma^2}} H_i\left(\frac{x}{x_0}\right) H_j\left(\frac{y}{y_0}\right), \quad (25)$$

where the σ is the beam size, H the Hermite polynomials, x_0 and y_0 are characteristic scales in the x and y directions.
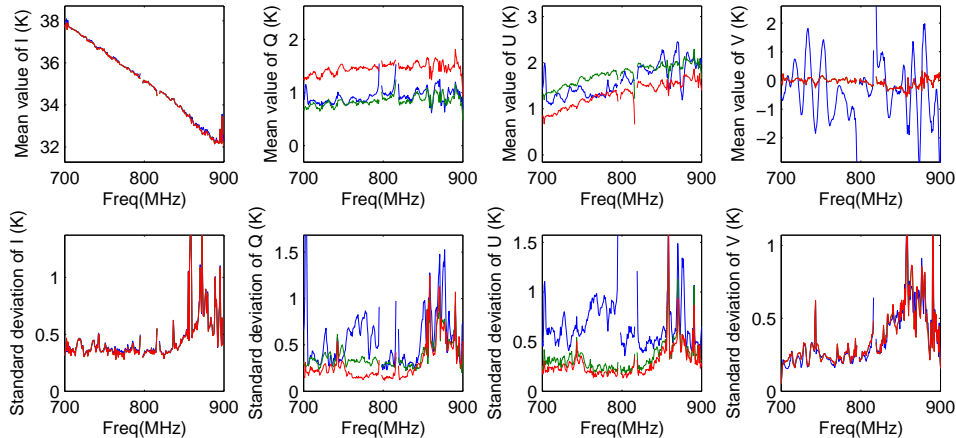
FIG. 7.— Calibrated 3C286 data. The upper panels show calibrated Stokes parameters averaged over 57 tracking scans on 3C286, while the lower ones show the standard deviations between those tracking scans. The blue lines show the result of calibration with parameters solved from pulsar data, the green lines correspond to calibration with modified θ_- and ϵ_- (based on 3C48 data), and the calibration shown as red lines using exactly same parameters except additional ionospheric Rotation Measure correction.
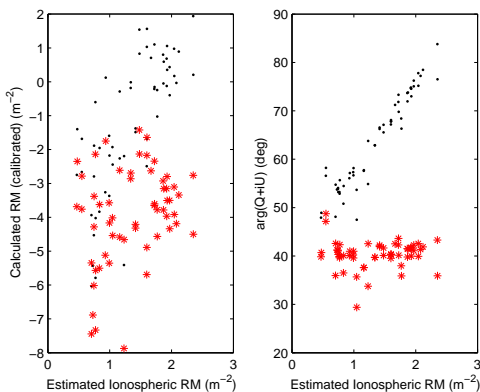

FIG. 8.— Comparison of linear polarization angle of 3C286 with (red asterisks) and without (black dots) ionospheric RM correction. The left panel shows the RM values fitted as the slope of linear polarization angles with respect to λ^2 using calibrated 3C286 data. The right panel are the phase angles of calibrated $Q + iU$ averaged over frequency channels. The x-axes are ionospheric RM values estimated with US-TEC model. The correlation coefficient r between x-axis and y-axis values of black dots, which show the results before RM correction, is 0.73 in the left panel and 0.95 in the right one. The correlation coefficients become 0.29 and 0.02, respectively, after applying RM correction. As shown here, the RM correction significantly reduces the variance and the averaged values of polarization angles of 3C286.

The Gauss-Hermite fit is then

$$S_{(I,Q,U,V)}(x,y) = \sum_{i=0}^{n} \sum_{j=0}^{n} a_{(I,Q,U,V),ij} \mu_{ij} \left(\frac{x}{x_0}, \frac{y}{y_0} \right),$$
(26)

where $a_{(I,Q,U,V),ij}$ are fitting coefficients.

We choose $n = 2$ to avoid over-fitting. σ is set to be the best-fit Gaussian beam size σ_g of I, and $x_0 = y_0 = \sigma_g$. The lower panels of Figure 9 show the best fit $S_{I,Q,U,V}$.

The most prominent feature of the derived polarized beam patterns is the dipole shape of the Stokes V beam. The dipole peak and trough are $\approx 12\%$ of the intensity at beam center. The dipole pattern in V is expected due to the off-axis design of the GBT (Srikanth 2012).

4.1.2. *Q-V and U-V coupling*

We further discover that the derived Q and U beam patterns show similar dipole shapes as the V beam, albeit at a lower level. Eqn. (A2) indicates that the errors in ϵ_+ and φ may induce leakage from V to Q and U, respectively. Eqn. (A2) also implies that ϵ_+ and φ are not easy to be constrained solely from unpolarized sources because these two parameters are absent in the first column of the first order approximation of δM, which describes the response of an unpolarized source. Therefore, we suspect that the Q and U beam dipole patterns may be due to leakage from the dipole pattern of V into Q/U, introduced by imperfect ϵ_+ and φ parameters we use in the boresight calibration stage, as described in Section 4.1.1

We quantify the Q-V and U-V linear correlations below to test this hypothesis. We fit a linear regression model to the calibration spider scan data in the form of $Q(x,y) + iU(x,y) = c + \tau V(x,y) + r(x,y)$, where c and τ are a constant and the complex linear coefficients, respectively, and r the residual. τ describes the leakage fraction, $\tau = \delta M_{2,4} + i\delta M_{3,4}$ in Eqn. (A2). The blue and green lines in Figure 10 show the real and imaginary part of τ, respectively.

4.1.3. *U-V Correction*

These relations could be intrinsic. They could also come from inappropriate polarization calibration. The red line in Figure 10 indicates the assumed argument of $(U_{\rm ncal} + iV_{\rm ncal})$ derived from the noise diode Stokes parameters yielded by the analysis of the pulsar observations using the PSRCHIVE tools. There is a strong correlation between the slope of the linear U-V relation (the imaginary part of τ) and the PSRCHIVE-derived noise diode argument.

As discussed in Section 3.2, we assume a noise diode frequency profile $\boldsymbol{S}_{\rm ncal}(\nu)$ to solve for G, γ, and φ for each observing session. Looking at the third and fourth rows of Eqn. (20), it can be shown that $\varphi = 0.5 \times \arg[(U'_{\rm ncal} + iV'_{\rm ncal})/(U_{\rm ncal} + iV_{\rm ncal})]$. Combined with Eqn. (A2), one can see that a biased $\delta \arg(U_{\rm ncal} + iV_{\rm ncal})$ will lead to

a $\delta U = V \times \delta \arg(U_{\mathrm{ncal}} + iV_{\mathrm{ncal}})$. Therefore, the strong correlation between $\arg(U_{\mathrm{ncal}} + iV_{\mathrm{ncal}})$ and the imaginary part of τ implies that $\delta \arg(U_{\mathrm{ncal}} + iV_{\mathrm{ncal}})$ is responsible for the correlation between U and V. In fact, after setting $\arg(U_{\mathrm{ncal}} + iV_{\mathrm{ncal}}) = 0$, the correlation between the U and V beam disappears.

4.1.4. Q-V Correction

On the other hand, the Q-V relation could be also from errors in the derived Mueller matrix parameters. Assuming errors in ϵ_+ is the only source of the observed Q-V coupling in spider scan data, we estimate $\delta\epsilon_+$ from 3C295 spider scan data, and apply the 'corrected' ϵ_+ to spider scan data of other unpolarized sources, including 3C147 and 3C295. It appears that the dipole features in Q are removed by the correction of ϵ_+.

However, the removal of dipole shapes in Q does not answer the question: Does the dipole shape come from leakage of V to Q due to $\delta\epsilon_+$? Or is it an intrinsic beam feature? To distinguish these two possible scenarios, we apply the modified ϵ_+ to the polarized 3C286 data.

The linear polarization fraction of 3C286 is $\sim 5\%$, and the circular polarization is negligible. One can expect that $\delta\epsilon_+$ mainly influences V in the calibrated 3C286 data. Comparing the RMS of V over tracking scans with different parallactic and Faraday rotation angles, we may have a handle on the origin of the Q-V coupling. We use 57 scans of 3C286 taken in 2011 to perform the test. The angles of rotation ϕ caused by sky rotation and ionospheric Faraday rotation range between $-88.4°$ to $60.6°$. We calculate $\sigma_V(\nu)$, the RMS of calibrated V over 57 tracking scans at each frequency channel, discard the highest 10% $\sigma_V(\nu)$ values to minimize impact of RFI and calculate the mean values. With ϵ_+ derived from pulsars and subsequently modified by spider scan data, the mean value of σ_V reduces from $0.752\% \pm 0.016\%$ to $0.716\% \pm 0.018\%$. The improvement appears marginal.

Figure 9 shows examples of the polarization beam pattern obtained from quasar spider scans, after correcting the φ and ϵ_+ parameters. In addition to the dipole pattern in the V beam, the Q and U beams show a less prominent quadrupole feature in the frequency range of 750-850 MHz. The amplitudes of these features are plotted as a function of frequency in Figure 11.

4.2. Polarization Beam from Pulsar tracking scans

Unpolarized quasar data provide useful information on the first column of $\mathbf{M}(\Delta\vec{x})$, and polarized sources are required in order to characterize the entire Mueller matrix. However, polarized quasars, such as 3C286 with a polarization fraction of about 5%, cannot provide significant signatures. For example, the expected leakage beam pattern from Q to I, according to the measured Mueller matrix model, is about 2%. With parallactic angle rotation, the change in Q of a 5% linearly polarized source is no greater than 10% of total intensity. The signature of Q leakage to I is therefore 0.2% at most, below our calibration significance of 0.6%. Furthermore, variations of the diffuse Galactic foreground radiation in the primary beam can contaminate the observation; it is difficult to completely separate quasar signals from the diffuse foreground, given a primary beam FWHM of 15' at 800 MHz at the GBT. We therefore solve for the full Mueller ma-

trix parameters of the primary beam with off-source pulsar data; by subtracting off-pulse phase bins from the on-pulse data, we mitigate the diffuse background while preserving the pulsar signals.

Assuming a known pulsar profile, we solve for the full Mueller matrix with the primary beam pattern $\mathbf{M}(\Delta\vec{x})$ at discrete positions, $\vec{x_0}$, assuming $\boldsymbol{S}(\vec{x'})$ is a delta function peaking at $\vec{x_0}$ in Eqn. (3).

We take 59 tracking scans of pulsar B1133+16, including 27 on-source tracking scans, and 32 off-centered ones with positions spread within a 0.19° radius from the beam center. The radius of 0.19° is about 0.7 times the beam FWHM at 800 MHz. The B1133+16 pulsar profile is obtained from multiple parallactic angle observations as described in Section 3.2 and use PSRCHIVE matrix template matching mode described in van Straten (2006) and van Straten (2013) to solve for the Mueller matrix parameters for each on- and off-source tracking scan. We allow θ_0 to vary to account for possible relative Q-U rotation between beam center and other parts of the beam.

After solving the Mueller parameters at 33 locations (one on-source and 32 off-centered ones), we again perform a 2D Gauss-Hermite fit (Eqn. (25)) to model the beam. Due to observational noise and variations of the pulsar profile itself, we are not able to model at high confidence level the beam pattern for individual channels. Instead, we average the Mueller parameters over the frequency range 755-845 MHz for the Gauss-Hermite fitting.

Figure 12 shows the Mueller matrix beam calculated with best fit results of parameters. As 3C295 is unpolarized, the first column of Figure 12 correspond to spider scan results on 3C295. Comparing Figure 9 and Figure 12, we find similar beam patterns with leakage derived from pulsar data and quasar spider scans.

To verify the goodness of fit, we perform a 'significance test' on each Jones matrix parameter. We simulate 33 sets of Mueller parameters, each with a normal distribution and a zero mean, and randomly assign them to the 33 locations. We again perform the 2D Gauss-Hermite fits, and record $R^2 \equiv 1 - (\sigma_{\mathrm{residual}}/\sigma_{\mathrm{data}})^2$, where σ_{data} and $\sigma_{\mathrm{residual}}$ are the standard deviations of the 33 simulated input and fitted parameters, respectively. With 500 such simulations, we derive the probability $P(R^2)$ that random parameters get better fitting results. It appears only the ϵ_- fit, which describes the dominant Stokes I to V leakage, is significant ($P < 5\%$). Although γ and θ_- show similar patterns as Q and U, respectively, they do not pass the significance test.

According to the spider scans, the expected patterns of Stokes I leakage into Q and U are less than one sixth in amplitude of Stokes I leakage into V, and are comparable to the uncertainty of polarization fraction of pulsar B1133+16, as shown in Figure 3. Therefore, it is not entirely surprising that we cannot detect significant patterns of γ and θ_-. Pulsar B0450+55 also shows a similar level of fluctuations in polarization fraction, unfortunately.

5. PROCEDURE OF ON-AXIS POLARIZATION CALIBRATION

The essential task for on-axis polarization calibration in this work is determining the parameters G, γ, φ, θ_-,
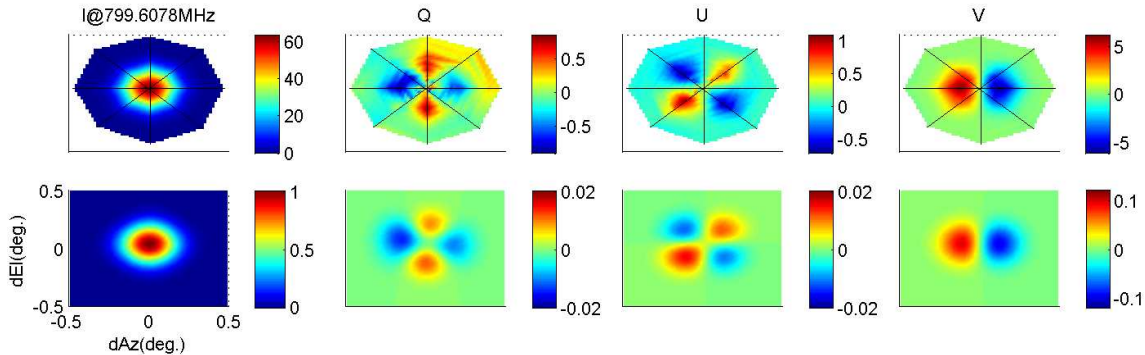
FIG. 9.— Polarized beam pattern at 800 MHz derived from spider scans of 3C295. The patterns in the upper panels are linear interpolation over the calibrated data of the spider scan, and the lower ones show the best fit results of the Gauss-Hermite model. The color scales of the upper panels are temperature in units of Kelvin, while the lower panels show fractional intensity compared to central source 3C295. Note we use modified Mueller matrix parameters as described in Section 4.1.2 and 4.1.4. As a result, the dipole patterns in the Q and U beams, first reported in Section 4.1.2, have been mitigated in this figure.
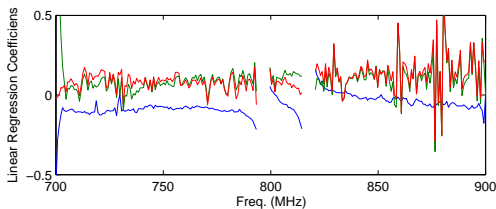

FIG. 10.— Q-V and U-V correlations in spider scan data. The blue and green lines show the real and imaginary part of τ. They also correspond to the Q-V and U-V correlations, respectively (see discussions in Section 4.1.2). The red line indicates the pre-assumed $\arg(U + iV)$ of the noise diode, which is used to calibrate φ for each night.
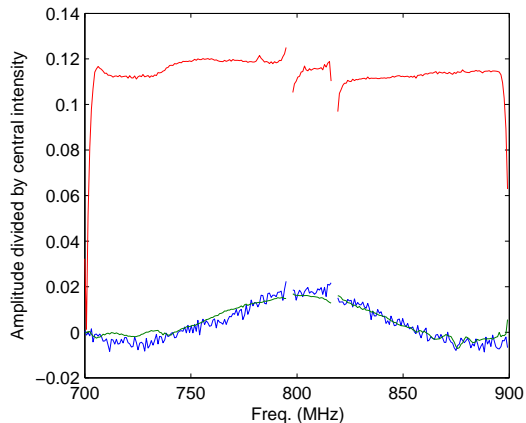

FIG. 11.— Coefficients of spider scan beam maps including quadrupole term of Q(blue), quadrupole term of U(green) and dipole term of V(red). The coefficients here are normalized by the peak value of I beam, and averaged over 7 spider scans on 3C48, 3C147, and 3C295.

ϵ_+ and ϵ_- as functions of time, and $\phi_{\rm RM}$ as function of time, azimuth, and elevation. Here we will summarize the methodology we adopt to determine these parameters.

1. Estimate noise diode frequency profile for each session with data of on/off source tracking scans on unpolarized quasars, like 3C48, 3C147, and 3C295 (Section 3.3.2).

2. Estimate G and γ by comparing observed noise diode data with estimated noise diode profile (Section 3.2.2).

3. Estimate φ from observed $\arg(U'_{\rm ncal} + iV'_{\rm ncal})$ of noise diode with assumed $V_{\rm ncal} = 0$ in real noise diode signal. (Section 4.1.3).

4. Apply G, γ, and φ to calibrate unpolarized quasar data (with the other parameters set to be 0). Then modify γ, θ_-, and ϵ_- based on quasar data calibrated in this step (Section 3.3.3).

5. Apply G, φ, along with modified γ, θ_-, and ϵ_- to calibrate spider scan data on another unpolarized quasar. Then estimate ϵ_+ with correlation between dipole features in Q and V data (Section 4.1.4).

6. Estimate $\phi_{\rm RM}$ with EOFs, US-TEC data, and IGRF. Then do ionospheric RM correction accordingly (Section 3.4).

6. DISCUSSION AND CONCLUSION

In this paper, we present the polarization calibration methodology for the GBT HI intensity mapping experiment. Accurate polarization calibration is critical to properly mitigate the unwanted leakage from polarized synchrotron foregrounds into total intensity.

We use multiple parallactic angle pulsar observations to solve for the six Jones Matrix parameters at boresight in each of the 256 frequency channels between 700-900 MHz at the GBT. Applying the solutions to unpolarized quasar observations, the RMS fluctuations of the Stokes parameters over time are about 1.3%-1.7% of total intensity. As a first-order correction, some of the Jones Matrix parameters are further modified based on tracking and spider scans of quasars. The RMS fluctuation reduces to 0.6%-0.8% of total intensity after the correction.

In Section 3.2 we discuss that there are two ways to break the degeneracy between I and V in PSRCHIVE: One assumes V to be negligible while observing a standard calibrator, i.e., the sum of V from the astrophysical calibrator, the (diffuse) sky, and the system, is negligible. However, the ϵ_- parameter obtained from PSRCHIVE
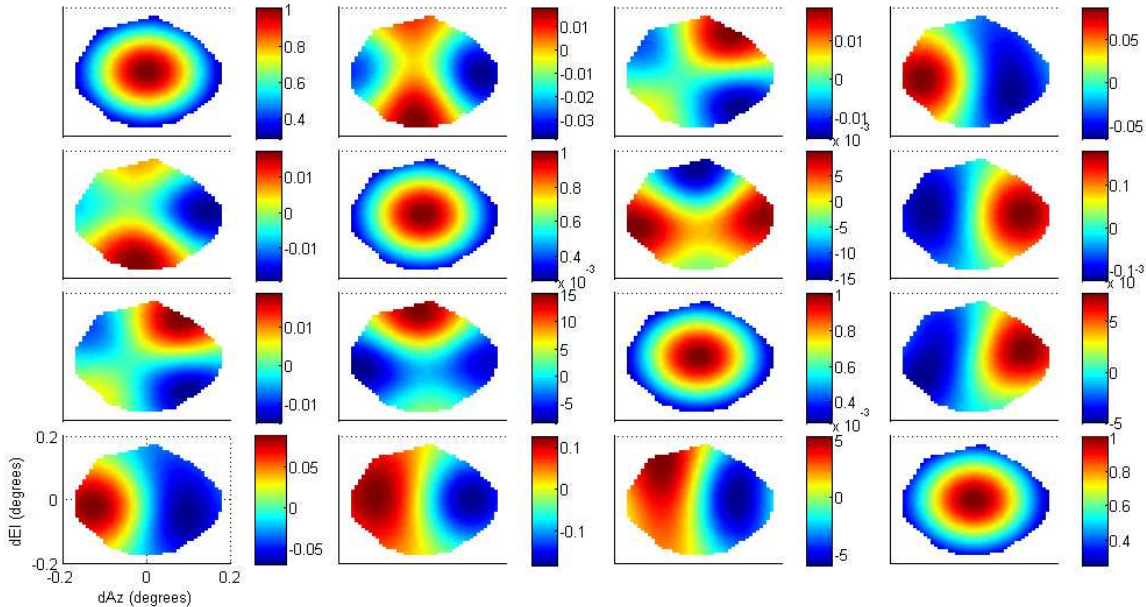
FIG. 12.— Beam pattern of the 4×4 Mueller matrix elements fitted with off-centered pulsar tracking scans. The diagonal elements are normalized to one, and from top-left to bottom-right the diagonal panels correspond to $M_{II}, M_{QQ}, M_{UU}, M_{VV}$, respectively.

under this assumption, which mainly describes the leakage between I and V, appears to be incorrect. This assumption does not seem to be valid in our case.

The other approach is to assume the V/U ratio of the noise diode is known. Section 4.1.2 and Figure 10 suggest that this could be a good assumption. However, PSRCHIVE assumes the noise diode signal is injected early in the system so that it shares the same light path as the sky signal; this is not the case for our GBT 800MHz observations, since the noise diode signal is injected after the OMT as discussed in Section 2.

Another explanation for the imperfection might be the variation of polarized pulsar profiles. PSR B1133+16, one of the pulsars we use to solve the Jones Matrix parameters, has been reported to have "orthogonally polarized modes", which may be responsible for the variations in the integrated fractional polarization and position angle of the pulsar (Karastergiou et al. 2002). The polarized pulse or frequency profiles of pulsars can in general fluctuate due to the astrophysical complexity of the pulse mechanism, or interference of the interstellar medium.

The polarized frequency profiles of quasars are more stable. However, with high fractional linear polarization and non-negligible circular polarization, pulsars provide more information needed to solve for all the Jones matrix model parameters than quasars, which are usually slightly or not polarized. Some of the parameters, including φ, ϵ_+, and θ_+, cannot be constrained by unpolarized sources. We can determine θ_+ by comparing the calibrated polarization position angle of 3C286 with the known value, while φ can be constrained by a highly polarized noise diode, which is however found to contain an uncertain V/U spectrum. The ϵ parameter is not affected by the noise diode as the signal injection takes place after the dipole receptor in the signal stream at the GBT.

Off-centered polarization leakage is also an important source of contamination. With quasar spider scans, we find a dominant dipole feature in the Stokes I to V leakage pattern, which is at the $\approx 12\%$ level, and secondary quadrupole features of Stokes I to Q and I to U leakage patterns, which are $\lesssim 2\%$ of total intensity. With the leakage of V dipole feature into Q and U, we can estimate $\delta\varphi$ and $\delta\epsilon_+$, and improve the calibration of polarized sources, like 3C286. Although there are still potential intrinsic dipole features in Q and U beam pattern which have yet to be separated from leakage of U.

We find similar features using off-centered pulsar observations and map out the entire Mueller matrix primary beam. However, the Stokes I to V leakage appears to be the only significantly determined beam pattern. The beam features of I leakage to Q and U are comparable to the variation of polarization profile of PSR B1133+16. Therefore, it is not surprising that we cannot significantly measure these features in the pulsar data.

In this paper, we measured the RMS fluctuations of calibrated on-source data of quasars, including unpolarized 3C48, 3C295, and 3C147, and slightly polarized 3C286, to be 0.6-0.8% of the total intensity. We also mapped the polarization beam pattern. Accurate polarization calibration at this level is required to mitigate the polarized foreground contribution for HI intensity mapping power spectrum measurements. We will report improvements on the redshifted HI power spectrum in future work. We will also investigate the Faraday rotation measure (RM) synthesis of Galactic foregrounds in the HI intensity mapping fields.

APPENDIX

FIRST-ORDER APPROXIMATION OF THE POLARIZATION CALIBRATION ERROR

In the model we use, $\mathbf{J}$ is a function of seven Jones matrix parameters, which can be rewritten as $\mathbf{J}(\vec{p})$, where $\vec{p} = \{p_i\} = \{G, \gamma, \varphi, \theta_+, \theta_-, \epsilon_+, \epsilon_-\}$ is the parameter vector. ϵ_+ and ϵ_- are defined as $\epsilon_+ = \epsilon_0 + \epsilon_1$ and $\epsilon_- = \epsilon_0 - \epsilon_1$. Mueller matrix can also be written as a function of these parameters $\mathbf{M}(\vec{p})$. See Section 3.1 for details.

Ideally, the polarization calibration should recover the real signal by applying inverse matrices of $\mathbf{M}$ and $\mathbf{R}(\phi)$ to Eqn. (3). However, if the estimated parameter vector $\vec{p'} = \vec{p} + \delta\vec{p}$ is slightly different from real parameter vector $\vec{p}$, the calibration procedure becomes

$$\begin{aligned}
\boldsymbol{S}''_{\rm sp} &= \mathbf{R}^{-1}\mathbf{M}(\vec{p'})^{-1}\boldsymbol{S}'_{\rm sp} \\
&= \mathbf{R}^{-1}\mathbf{M}(\vec{p'})^{-1}\mathbf{M}(\vec{p})\mathbf{R}\boldsymbol{S}_{\rm sp} \\
&= \boldsymbol{S}_{\rm sp} + \mathbf{R}^{-1}\delta\mathbf{M}\mathbf{R}\boldsymbol{S}_{\rm sp},
\end{aligned} \tag{A1}$$

where $\delta\mathbf{M} = \mathbf{M}(\vec{p'})^{-1}\mathbf{M}(\vec{p}) - \mathbf{I}$, $\mathbf{I}$ is the identity matrix. The term $\mathbf{R}^{-1}\delta\mathbf{M}\mathbf{R}\boldsymbol{S}_{\rm sp}$ is then the error introduced by the polarization calibration procedure.

If $\theta_+, \theta_-, \epsilon_0, \epsilon_1 \ll 1$, the first-order perturbation of $\mathbf{M}$ is

$$\delta\mathbf{M} \approx \begin{pmatrix} -2\delta G & -2\delta\gamma & -\delta\theta_- & \delta\epsilon_- \\ -2\delta\gamma & -2\delta G & 0 & \delta\epsilon_+ \\ -\delta\theta_- & 0 & -2\delta G & -2\delta\varphi \\ \delta\epsilon_- & -\delta\epsilon_+ & 2\delta\varphi & -2\delta G \end{pmatrix}. \tag{A2}$$

We can then write down the expression for the error,

$$\mathbf{R}^{-1}(\phi + \delta\phi)\delta\mathbf{M}\mathbf{R}(\phi) \approx$$

$$\begin{pmatrix} -2\delta G & -(2\delta\gamma\cos 2\phi - \delta\theta_-\sin 2\phi) & -\delta\theta_-\cos 2\phi - 2\delta\gamma\sin 2\phi & \delta\epsilon_- \\ -(2\delta\gamma\cos 2\phi - \delta\theta_-\sin 2\phi) & -2\delta G & -2\delta\phi & \delta\epsilon_+\cos 2\phi + 2\delta\varphi\sin 2\phi \\ -\delta\theta_-\cos 2\phi - 2\delta\gamma\sin 2\phi & 2\delta\phi & -2\delta G & \delta\epsilon_+\sin 2\phi - 2\delta\varphi\cos 2\phi \\ \delta\epsilon_- & -(\delta\epsilon_+\cos 2\phi + 2\delta\varphi\sin 2\phi) & -\delta\epsilon_+\sin 2\phi + 2\delta\varphi\cos 2\phi & -2\delta G \end{pmatrix}. \tag{A3}$$

The operator $\mathbf{R}$ can be combined with the effect of θ_+ (see section 3.1), so $\delta\theta_+$ behaves like $\delta\phi$ above.

REFERENCES

Araujo-Pradere, E. A., Fuller-Rowell, T. J., Spencer, P. S. J., Minter, C. F., 2007, Radio Science, 42, 3, DOI: 10.1029/2006RS003459.
Asad, K. M. B., et al., 2015, MNRAS, 451, 3709
Britton, M. C., 2000, ApJ, 532, 1240
Chang, T.-C., Pen, U.-L., Bandura, K., Peterson, J. B., 2010, Nature, 466, 463
Chang, T.-C., Pen, U.-L., 2008, PRL, 100, 091303
DuPlain, R., Ransom, S., Demorest, P., Brandt, P., Ford, J., Shelton, A. L., 2008, Proc. SPIE, 7019, 70191D
Finlay, C. C., et al., 2010, Geophys. J. Int., 183, 1216
Fuller-Rowell, T., Araujo-Pradere, E., Minter, C., Codrescu, M., Spencer, P., Robertson, D., Jacobson, A. R., 2006, Radio Science, 41, 6, DOI: 10.1029/2005RS003393.
Han, J. L., Demorest, P. B., van Straten, W., Lyne, A. G., 2009, ApJS, 181, 557
Heiles, C., 2001, PASP, 788, 1243
Hotan, A. W., van Straten, W., Manchester, R. N., 2004, PASA, 21, 302
Jelić V. et al., 2010, MNRAS, 409, 1647
Johnston, S., Hobbs, G., Vigeland, S., Kramer, M., Weisberg, J. M., Lyne, A. G., 2005, MNRAS, 364, 1397
Karastergiou, A., Kramer, M., Johnston, S., Lyne, A. G., Bhat, N. D. R., Gupta, Y., 2002, Astronomy and Astrophysics, 391, 247
Loeb, A., Wyithe, S., 2008, PRL, 100, 161301

Martí-Vidal, I., Krichbaum, T. P., Marscher, A., Alef, W., Bertarini, A., Bach, U., Schinzel, F. K., Rottmann, H., Anderson, J. M., Zensus, J. A., Bremer, M., Sanchez, S., Lindqvist, M., Mujunen, A., 2012, A&A, 542, A107
Masui, K. W., Switzer, E. R., Banavar, N., Bandura, K., Blake, C., Calin, L.-M., Chang, T.-C., Chen, X., Li, Y.-C., Liao, Y.-W., Natarajan, A., Pen, U.-L., Peterson, J. B., Shaw, J. R., Voytek, T. C., 2013, ApJ, 763, L20
Moore, D. F, Aguirre, J. E., Parsons, A. R., Jacobs, D. C, Pober, J. C., 2013, ApJ, 796, 154
Moore, D. F, et al., 2015, submitted to ApJ, arXiv:1502.05072
Oh, S. P., and Mack, K. J., 2003, MNRAS 346, 871
Perley, R. A., and Butler, B. J., 2013, ApJS, 206, 16
Srikanth, S., 2012, Personal Communication
Seo, H.-J., Dodelson, S., Marriner, J., Mcginnis, D., Stebbins, A., Stoughton, C., and Vallinotto, A., 2010, ApJ 721, 164
van Straten, W., 2004, ApJS, 152, 129
van Straten, W., 2006, ApJ, 642, 1004
van Straten, W., 2013, ApJS, 204, 13
Switzer, E. R., Masui, K. W., Bandura, K., Calin, L.-M., Chang, T.-C., Chen, X.-L., Li, Y.-C., Liao, Y.-W., Natarajan, A., Pen, U.-L., Peterson, J. B., Shaw, J. R., Voytek T. C., 2013, MNRAS, 434, L46